SCIENCE CHINA
Physics, Mechanics & Astronomy

• Article •

June 2014 Vol. 57 No. 6: 1178–1193
doi: 10.1007/s11433-014-5454-9

Competition of the multiple Görtler modes in hypersonic boundary layer flows†

REN Jie & FU Song*

School of Aerospace Engineering, Tsinghua University, Beijing 100084, China

Received February 17, 2014; accepted March 6, 2014; published online April 17, 2014

Competition of multiple Görtler modes in hypersonic boundary layer flows are investigated with the local and marching methods. The wall-layer mode (mode W) and the trapped-layer mode (mode T) both occur in the compressible boundary layer where there exists a temperature adjustment layer near the upper edge. The mode T has the largest growth rate at a lower Görtler number while the mode W dominates at larger Görtler numbers. These two modes are both responsible for the flow transition in the hypersonic flows especially when Görtler number is in the high value range in which the crossover of these two modes takes place. Such high Görtler numbers are virtually far beyond the neutral regime. The nonparallel base flows, therefore, cease to influence the stability behavior of the Görtler modes. The effects of the Mach number on the multiple Görtler modes are studied within a chosen Mach number of 0.95, 2, 4 and 6. When the flow Mach number is sufficiently large, e.g., $Ma \geqslant 4$, the growth rate crossover of the mode T and mode W occurs both in the conventional G-β map as well as on the route downstream for a fixed wavelength disturbance. Four particular regions (Region T, T-W, W-T and W) around the crossover point are highlighted with the marching analysis and the result matches that of the local analysis. The initial disturbance of a normal mode maintains the shape in its corresponding dominating region while a shape-transformation occurs outside this region.

Görtler vortices, linear stability theory, multiple modes, local analysis, marching analysis

PACS number(s): 47.20.Ft, 47.20.Ib, 47.20.Qr

Citation: Ren J, Fu S. Competition of the multiple Görtler modes in hypersonic boundary layer flows. Sci China-Phys Mech Astron, 2014, 57: 1178–1193, doi: 10.1007/s11433-014-5454-9

1 Introduction

Since Görtler's pioneering investigation [1] on the boundary layer instabilities subjected to the negative curvature in 1940 highlighting the existence of the streamwise-oriented counter-rotating vortices, extensive studies have been carried out on this subject especially in the incompressible flows. These vortices are caused by the imbalance between the centrifugal force and the normal pressure gradient near a concave surface and exhibit a quasi-constant spanwise wavelength. Görtler number, as will be defined later, is the critical non-dimensional parameter characterizing the degree of this imbalance. For earlier comprehensive reviews, the reader may refer to Herbert [2], Hall [3], Floryan [4] and Saric [5].

1.1 The neutral curve: local and marching analysis

In the category of linear stability, different neutral curves had been obtained in the past with the parallel flow assumption [6]. Some of the disagreements were due to computational errors while some due to the improper neglect of terms like streamwise derivatives. It was until Floryan and Saric's analysis [6,7] that the neutral curve was finally fixed with the local analysis approach. A critical Görtler number (hereafter referred to as G) of 0.4638 located at the quasi-zero spanwise wavenumber of the neutral curve was given. They also illustrated that the effect of curvature on the base flow could be

*Corresponding author (email: fs-dem@tsinghua.edu.cn)
†Contributed by FU Song (Associate Editor-in-Chief)

neglected.

Hall [8,9], nevertheless, reached an important conclusion that there is no unique neutral curve at the small wavenumber regime where the neutral stability is shown to depend on how and where the boundary layer is perturbed, say, the receptivity process. An asymptotic investigation with parallel flow assumption showed that only the first few terms in the expansion were retained. This is definitely insufficient when nonparallel effects became relevant. Therefore, the parallel-flow approximation universally applied had no mathematical justification except at high values of the spanwise wavenumber. In fact, it was in this large wavenumber regime that the different neutral curves merge and exhibit the asymptotic and parallel-flow behavior. Higher eigen states had also been noticed by Hall that the number of vortices increases with the mode level and, without exception, the most amplified disturbances correspond to the primary mode.

To adequately explore the feasibility of the local analysis on the Görtler instability, the local normal eigenvalue problem had been studied extensively. Day et al. [10] compared the local and marching solutions of the linear stability equations. They found that different initial conditions led to different routes towards the same eigensolution further downstream and concluded that the differences were modest. Bottaro and Luchini [11] also found that the asymptotic behavior far downstream is independent of the initial excitation. Goulpié et al. [12] paid special attention to the pressure gradient of the base flow using Falkner-Skan similarity solution. They applied both the local nonparallel analysis and the marching analysis and showed that the local method always gives a unique neutral curve as a well mathematically formulated problem. In fact, in the eigenvalue formations, a unique neutral curve can be drawn indicating that the perturbations of a forced wavelength begin to amplify without the consideration of where and how the disturbances were initiated. The asymptotic behavior of the neutral curve is given by Hall [9]. He found for $\alpha_x \ll 1, G_x \sim \alpha_x^{-2}$, whilst for $\alpha_x \gg 1, G_x \sim \alpha_x^4$. Here α_x and G_x are the local wavenumber and Görtler number defined by Hall. The relations between Hall's formulation and the present formulation (see sect. 2) are $\alpha_x = \beta$ and $G_x = 2G^2$. Thus, the asymptotic behavior of the neutral curve can be interpreted as $\beta \ll 1, G \sim \beta^{-1}$ and $\beta \gg 1, G \sim \beta^2$. The problem is, whether this neutral curve is tenable and in which regime the calculation is valid. As a result, the eigenvalue approach is valid either in the large wavenumber regime or far downstream of the neutral point, i.e., in the large G number regime.

As the initial condition for the development of perturbations, receptivity is a very important aspect of the Görtler instability. Recently, Wu et al. [13] formulated the initial-boundary-value problem describing the receptivity process as well as the development of the induced perturbation. A constant physical wavelength vortex was analyzed along the streamwise development and four distinct regimes were identified. Their analysis showed that the Görtler vortices can be effectively excited by free-stream vortical disturbances. In their local analysis, the inclusion of nonparallel features did not lead to an improved result.

1.2 Hypersonic and nonlinear effects

The nonparallel nature of boundary layer flows increases the complexity of the stability problem. Compressibility contributes to additional complexity on the resulting system. The stability and transition in compressible flows have been a critical issue recently due to their practical importance. The main path to the transition in the compressible boundary layer flows had been outlined, for instance, by Morkovin and highlighted by Fedorov [14] and Zhong and Wang [15]. For the unstable boundary layer flows including the first and the second modes, the crossflow instability and the Görtler instability, the transition path with the minimum ambient disturbance level represents the traditional path to turbulence with low disturbance environments where the modal growth is dominant. Along this path, the laminar flow experiences the excitation of the unstable normal modes (receptivity problem), the downstream amplification (linear and nonlinear) and the final breakdown.

Studies of the Görtler instability in the compressible boundary layers have been reported by a number of researchers. The most distinct difference between the incompressible counterpart is the existence of a temperature adjustment layer near the upper edge of the boundary layer where the temperature decays from $O(Ma^2)$ to the freestream value [16]. Dando and Seddougui [17] identified the "trapped-layer mode" for large wavenumbers and the "adjustment-layer mode" for large Mach numbers apart from the conventional "wall layer mode" (mode W) observed in the incompressible cases. In fact, the two new modes are equivalent and will be named as trapped-layer mode (mode T) in this article. The crossover of the mode W and mode T has been observed in their study but with unit Prandtl number and Chapman viscosity law approximations.

Li et al. [18] examined the nonlinear development of the Görtler vortices in high-speed boundary layers including the breakdown via high-frequency secondary instabilities and Görtler-second mode interactions. As pointed out by the authors, in the supersonic and hypersonic transition flow, the Görtler instability becomes even more relevant. Hall and Fu [19] demonstrated that the neutral curve at hypersonic condition has distinct left and right branches and a unique minimum. They showed that the neutral curve can be described by a quasi-parallel theory. The destabilizing effects of Görtler vortices, wall cooling and gas dissociation on the Rayleigh secondary instability in the hypersonic boundary layer were also shown [20].

Hall and Malik [21] applied the asymptotic methods with the nonparallel effects considered. They obtained the right branch of the neutral curves for Ma =2, 4 and 6, respectively, although the small-wavenumber region is likely outside the

range of validity of the theory. Spall and Malik [22] solved the parabolized stability equations at $O(1)$ wavelength with a finite-difference approach. Their results showed that all growth rate curves merged along the streamwise direction. Receptivity of Görtler vortices in hypersonic boundary layers were reported by Whang and Zhong [23,24] showing that the Görtler vortices are mainly induced by freestream standing vortices.

Along with the experiment conducted by Swearingen and Blackwelder [25], the numerical study of the nonlinear Görtler stability had drawn the attention of Hall [26], Sabry and Liu [27], Lee and Liu [28] and Li and Malik [29] in the early 1990s. Their calculation showed good agreement at early stages with the experiment. Hall [26] calculated the nonlinear problem with eight Fourier modes and pointed out that the nonparallel effects were important in the nonlinear regime for the whole wavenumber. It was suggested that the nonlinear effects were to prevent the exponential growth. The nonlinear evolution of the vortices developed inflectional profiles that may be receptive to the secondary Rayleigh instability. Sabry and Liu [27] investigated the Görtler instability especially in the nonlinear regime with detailed discussions on the effects of initial conditions. Lee and Liu [28] solved the parabolized PDE using SIMPLE algorithm and the sensitivity to the set-in point of the initial disturbances was also discussed. Li and Malik [29] focused on the secondary instability. They found that the even mode (lead to varicose mode breakdown) was stronger for the large wavelengths while the odd mode (lead to sinuous mode breakdown) was stronger for the short wavelengths.

More recently, Tandiono et al. [30] focused on the spanwise velocity component of the Görtler flow with hot-wire anemometer measurement. Kim et al. [31] investigated the onset of the Görtler vortices and derived a higher critical Görtler number as compared with the existing experiment and theoretical results. Schrader et al. [32], in their DNS, simulated the receptivity, disturbance growth and breakdown in the boundary layer transition flows. Experimental and theoretical studies on both the steady and unsteady Görtler instabilities are reported by Boiko et al. [33] where good agreement between experiment and numerical calculation is obtained. The most dangerous four modes of the secondary instability of Görtler vortices are investigated by Ren and Fu using Floquet analysis [34]. All these studies fall in the scope of incompressible flows. Nevertheless, the Görtler stability problem is a historical topic with emerging new issues especially in compressible flows.

1.3 Motivation of the present work

Though the crossover of the growth rate for the mode T and mode W had been given by Dando et al. [17]. It should be noted that most of the existing studies focus on the Görtler vortices generated by a single mode (usually the primary Görtler mode), multiple Görtler modes have rarely been investigated apart from the incompressible studies by Herbert [35] (through temporal analysis) and by Floryan [36] (with spatial analysis). These work illustrated that the growth rate of the second Görtler mode is much slower than that of the first one over the entire wavelength in their studies. Even so, Herbert [35] speculated that "*higher eigenstates of Görtler vortices may well be important in laminar–turbulent transition*" while Floryan [36] argued that "*the growth process of the second mode is considerably slower than that of the first; therefore, the second mode is not likely to be observed experimentally*". As also commented by Spall and Malik [22], it is important to find out which mode will dominate the transition in hypersonic boundary layer flows. The present work is, thus, aiming at this point in an attempt to clarify the behavior of the multiple Görtler modes on the compressible boundary layer flows with both the local method and the marching method that solves the parabolic equations directly. Here, the local analysis helps to identify the unstable modes and predicts their downstream growth. It was illustrated [23,24] that the local analysis and DNS results agreed well showing the hypersonic Görtler vortices can be well captured with the local analysis in the linear regime. As will be illustrated here, the local analysis gives reliable results for $G > O(1)$, say, downstream of the neutral regime.

The study of the Görtler instability, especially for incompressible flows, had been based on the assumptions of large Reynolds number ($Re \to \infty$) and small curvature ($k \to 0$). The key nondimensional parameter is G only. From Herbert's result [35], the omitted curvature and Re related terms have a significant effect on the neutral regime and the critical G value is never located at $\beta \to 0$ if the assumption $k \to 0$ is abandoned. In the present study, the Re and k related terms are retained. In the stability equations of the compressible flows, Mach number Ma along with the Reynolds number Re and the curvature k is also an important flow parameter characterizing the flow instability behavior. For the sake of comparison with the existing results, the neutral curve is acquired in the G-β and G-Λ maps to distinguish the stable and unstable flow regions. The definition of the spanwise wavenumber β and the wavenumber parameter Λ can be found in §2 and 3.

The present study will illustrate, for the hypersonic flows, through the local and marching analysis, the crossover of the mode W and the mode T at $O(1)$ wavenumber and large Görtler number regime. In fact, it is at this wavenumber regime that the instability is most likely to occur. The two approaches are expected to deliver similar results but the marching analysis helps to express the details of the crossover and confirm the result of the local analysis.

2 Mathematical formulation of the local and marching analysis

2.1 The Basic flow

Starting from the compressible Navier-Stokes (hereafter referred to as N-S) equations, the governing equations for

Görtler vortices can be derived in the following manner. The primary N-S equations are

$$\frac{\partial \rho^*}{\partial t^*} + \nabla^* \cdot (\rho^* \boldsymbol{V}^*) = 0, \tag{1a}$$

$$l\rho^* \left(\frac{\partial \boldsymbol{V}^*}{\partial t^*} + (\boldsymbol{V}^* \cdot \nabla^*) \boldsymbol{V}^* \right) = -\nabla^* p^* + \nabla^* (\lambda^* (\nabla^* \cdot \boldsymbol{V}^*)) + \nabla^* \cdot \left(\mu^* \left(\nabla^* \boldsymbol{V}^* + \nabla^* \boldsymbol{V}^{*T} \right) \right), \tag{1b}$$

$$l\rho^* C_p{}^* \left(\frac{\partial T^*}{\partial t^*} + (\boldsymbol{V}^* \cdot \nabla^*) T^* \right) = \nabla^* \cdot (\kappa^* \nabla^* T^*) + \frac{\partial p^*}{\partial t^*} + (\boldsymbol{V}^* \cdot \nabla^*) p^* + \Phi^*, \tag{1c}$$

where the viscous dissipation function in the energy equation (1c) is

$$\Phi^* = \lambda^* (\nabla^* \cdot \boldsymbol{V}^*)^2 + \frac{\mu^*}{2} \left(\nabla^* \boldsymbol{V}^* + \nabla^* \boldsymbol{V}^{*T} \right)^2. \tag{2}$$

The asterisk denotes the dimensional quantities in this article. The compressible boundary layer flow over a concave wall with a constant streamwise curvature k^* is considered. The orthogonal curvilinear coordinate system in Figure 1 is employed in the formulation. Here, the coordinate x is along the streamwise direction, y normal to the wall and z in the spanwise direction.

The velocity components u^*, v^*, w^* are non-dimensionalized with the far-field potential velocity U_∞^* (subscript ∞ is used for potential flow quantities), the density ρ^*, temperature T^*, dynamic viscosity μ^*, second viscosity λ^* and thermal conductivity κ^* with their respective free stream values and pressure p^* by $\rho_\infty^* U_\infty^{*2}$, i.e.,

$$u = \frac{u^*}{U_\infty^*}, v = \frac{v^*}{U_\infty^*}, w = \frac{w^*}{U_\infty^*}, p = \frac{p^*}{\rho_\infty^* (U_\infty^*)^2}, \quad \rho = \frac{\rho^*}{\rho_\infty^*}, T = \frac{T^*}{T_\infty^*}, \mu = \frac{\mu^*}{\mu_\infty^*}, \lambda = \frac{\lambda^*}{\lambda_\infty^*}, \kappa = \frac{\kappa^*}{\kappa_\infty^*}. \tag{3}$$

The length and curvature are scaled by the boundary layer length scale $\delta_0^* = \sqrt{\nu_\infty^* x_0^* / U_\infty^*}$ and the time scaled by δ_0^*/U_∞^*, i.e.,

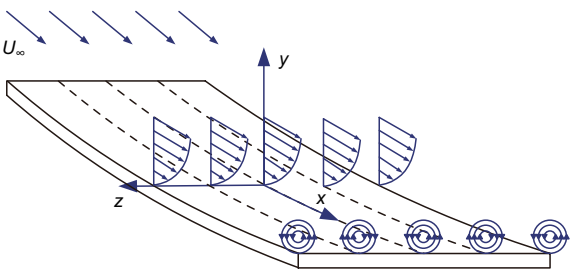

Figure 1 (Color online) Illustration of the orthogonal curvilinear coordinates for the Görtler instability analysis.

$$x = \frac{x^*}{\delta_0^*}, y = \frac{y^*}{\delta_0^*}, z = \frac{z^*}{\delta_0^*}, k = k^* \delta_0^*, t = \frac{t^* U_\infty^*}{\delta_0^*}. \tag{4}$$

Here, x_0^* is the x-coordinate of a specified location. In the local method, x_0^* is the station where the normal mode decomposition is applied. In the marching method, x_0^* is the station where initial conditions are specified. The N-S equations are supplemented with the relations below.

Equation of state

$$p^* = \rho^* R^* T^* \Leftrightarrow p = \frac{\rho T}{\gamma M a^2}. \tag{5}$$

Sutherland law

$$\mu^* = \mu_s^* \frac{T^*}{T_s^*} \frac{T_s^* + S^*}{T^* + S^*} \Leftrightarrow \mu = \mu_s \frac{T}{T_s} \frac{T_s + S}{T + S}. \tag{6}$$

$T_s^* = 273$ K, $\mu_s^* = 1.71 \times 10^{-5}$ kg/(m·s), $S^* = 110.4$ K.

Stokes's hypothesis

$$\lambda^* + 2/3\mu^* = 0 \Leftrightarrow \lambda = -2/3\mu. \tag{7}$$

Calorically perfect gas

$$C_p^* = \text{const}, R^* = \text{const}. \tag{8}$$

Constant Pr

$$Pr = \frac{C_p{}^* \mu^*}{\kappa^*} = \text{const} \Leftrightarrow \mu = \kappa. \tag{9}$$

In the calculation of the base flow, the curvature related terms were neglected as discussed by Floryan [6]. The compressible flow over a flat plate with zero streamwise pressure gradients is computed as a self-similar solution to the boundary layer equations [37].

2.2 The stability equations of the disturbances

The disturbance equations are obtained through the decomposition of the flow quantities $\tilde{q} = \left(\tilde{\rho}, \tilde{u}, \tilde{v}, \tilde{w}, \tilde{T} \right)$ into the perturbation $\tilde{q}$ as well as the primary state q_0 which were just solved as the base flow. Thus,

$$q(x, y, z, t) = q_0(x, y) + \tilde{q}(x, y, z, t). \tag{10}$$

The tilde symbol denotes the perturbed flow quantities. Substitute eq. (10) into the full N-S equations (1), the base flow equations are then subtracted. The disturbance equations are presented below in a compact form after the nondimensional procedure as given in equations eqs. (3) and (4):

$$\boldsymbol{\Gamma} \frac{\partial \tilde{q}}{\partial t} + \boldsymbol{A} \frac{\partial \tilde{q}}{\partial x} + \boldsymbol{B} \frac{\partial \tilde{q}}{\partial y} + \boldsymbol{C} \frac{\partial \tilde{q}}{\partial z} + \boldsymbol{D} \tilde{q} = \boldsymbol{H}_{xx} \frac{\partial^2 \tilde{q}}{\partial x^2} + \boldsymbol{H}_{xy} \frac{\partial^2 \tilde{q}}{\partial x \partial y} + \boldsymbol{H}_{xz} \frac{\partial^2 \tilde{q}}{\partial x z} + \boldsymbol{H}_{yy} \frac{\partial^2 \tilde{q}}{\partial y^2} + \boldsymbol{H}_{yz} \frac{\partial^2 \tilde{q}}{\partial y \partial z} + \boldsymbol{H}_{zz} \frac{\partial^2 \tilde{q}}{\partial z^2} + N. \tag{11}$$

Matrices (5×5) $\boldsymbol{\Gamma}$, $\boldsymbol{A}$, $\boldsymbol{B}$, $\boldsymbol{C}$, $\boldsymbol{D}$, $\boldsymbol{H}_{xx}$, $\boldsymbol{H}_{yy}$, $\boldsymbol{H}_{zz}$, $\boldsymbol{H}_{xy}$, $\boldsymbol{H}_{yz}$ and $\boldsymbol{H}_{xz}$ represent the coefficients that are functions of the Re, Ma, Pr

numbers, curvature and base flow quantities (see Appendix). These nondimensional numbers are defined as:

$$Re = \frac{\rho_\infty^* U_\infty^* \delta_0^*}{\mu_\infty^*}, Ma = \frac{U_\infty^*}{\sqrt{\gamma R_{\text{air}}^* T_\infty^*}}, Pr = \frac{\mu_\infty^* C_p^*}{\kappa_\infty^*}. \tag{12}$$

Nonlinear terms are denoted by the vector N. The definition of G is given as:

$$G = Re\sqrt{k}. \tag{13}$$

The disturbances and nonlinear terms are expressed by the truncated Fourier series:

$$\tilde{q}(x,y,z,t) = \sum_{m=-M}^{M}\sum_{n=-N}^{N} \hat{\varphi}_{mn}(x,y)\exp(\mathrm{i}n\beta z - \mathrm{i}m\omega t), \tag{14}$$

$$N = \sum_{m=-M}^{M}\sum_{n=-N}^{N} \hat{F}_{mn}\exp(\mathrm{i}n\beta z - \mathrm{i}m\omega t), \tag{15}$$

where β is the spanwise wavenumber and ω the frequency. Substitute eqs. (14) and (15) into eq. (11), the governing equations for the shape functions of each Fourier mode are derived

$$\begin{aligned}&\boldsymbol{H}_x\frac{\partial\hat{\varphi}_{mn}}{\partial x} + \boldsymbol{H}_y\frac{\partial\hat{\varphi}_{mn}}{\partial y} + \boldsymbol{H}\hat{\varphi}_{mn}\\ &= \boldsymbol{H}_{xx}\frac{\partial^2\hat{\varphi}_{mn}}{\partial x^2} + \boldsymbol{H}_{xy}\frac{\partial^2\hat{\varphi}_{mn}}{\partial x\partial y} + \boldsymbol{H}_{yy}\frac{\partial^2\hat{\varphi}_{mn}}{\partial y^2} + \hat{F}_{mn}.\end{aligned} \tag{16}$$

The matrices $\boldsymbol{H}_x$, $\boldsymbol{H}_y$ and $\boldsymbol{H}$ are given by

$$\boldsymbol{H}_x = \boldsymbol{A} - \mathrm{i}n\beta\boldsymbol{H}_{xz}, \tag{17a}$$

$$\boldsymbol{H}_y = \boldsymbol{B} - \mathrm{i}n\beta\boldsymbol{H}_{yz}, \tag{17b}$$

$$\boldsymbol{H} = \boldsymbol{D} - \mathrm{i}m\omega\boldsymbol{\Gamma} + \mathrm{i}n\beta\boldsymbol{C} + \beta^2 n^2\boldsymbol{H}_{zz}. \tag{17c}$$

For the linearized equation of (11), the nonlinear expansions in eq. (15) are neglected. Here, we consider spatial stability problem with steady motion, i.e., $\omega \equiv 0$. Further solution procedure is given below in sect. 2.3.

In the local sense, the shape function is assumed to be independent of x, i.e.,

$$\tilde{q}(x,y,z,t) = \hat{\varphi}(y)\exp(\mathrm{i}\alpha x + \mathrm{i}\beta z - \mathrm{i}\omega t) + c.c. \tag{18}$$

Here, $c.c.$ denotes complex conjugate. The normal mode equation can then be expressed as:

$$\begin{aligned}&\left(-\mathrm{i}\omega\boldsymbol{\Gamma} + \mathrm{i}\beta\boldsymbol{C} + \boldsymbol{D} + \beta^2\boldsymbol{H}_{zz}\right)\hat{\varphi} + \left(\boldsymbol{B} - \mathrm{i}\beta\boldsymbol{H}_{yz}\right)\frac{\partial\hat{\varphi}}{\partial y} - \boldsymbol{H}_{yy}\frac{\partial^2\hat{\varphi}}{\partial y^2}\\ &= \alpha\left(-\mathrm{i}\boldsymbol{A}\hat{\varphi} - \beta\boldsymbol{H}_{xz}\hat{\varphi} + \mathrm{i}\boldsymbol{H}_{xy}\frac{\partial\hat{\varphi}}{\partial y}\right) - \alpha^2\boldsymbol{H}_{xx}\hat{\varphi},\end{aligned} \tag{19}$$

2.3 Outline of the numerical methods

The compressible Görtler instability equations derived in eqs. (16) and (19) are solved numerically with finite difference approach. Analysis of the magnitude of the coefficient matrices gives

$$\boldsymbol{\Gamma} \sim \boldsymbol{A} \sim \boldsymbol{B} \sim \boldsymbol{C} \sim \boldsymbol{D} \sim O(1), \tag{20a}$$

$$\boldsymbol{H}_{xx} \sim \boldsymbol{H}_{xy} \sim \boldsymbol{H}_{xz} \sim \boldsymbol{H}_{yy} \sim \boldsymbol{H}_{yz} \sim \boldsymbol{H}_{zz} \sim O\left(\frac{1}{Re}\right). \tag{20b}$$

This allows the simplification of eq. (16) into parabolic equations and eq. (19) into standard eigenvalue problem. Say, the partial differential terms respect to x: $\boldsymbol{H}_{xx}\frac{\partial^2\hat{\varphi}_{mn}}{\partial x^2}, \boldsymbol{H}_{xy}\frac{\partial^2\hat{\varphi}_{mn}}{\partial x\partial y}$ in eq. (16) and quadratic term $\alpha^2\boldsymbol{H}_{xx}\hat{\varphi}$ in eq. (19) can be neglected. In this manner, eq. (16) can be marched in the x-direction.

The disturbance vector $\hat{\Phi}$ to be solved is the group of $\hat{\varphi}$ defined below:

$$\hat{\Phi} = (\hat{\varphi}_1, \hat{\varphi}_2, \cdots \hat{\varphi}_N). \tag{21}$$

Here, the subscript denotes the index of grid points in the y-direction. The partial derivatives in eqs. (16) and (19) are replaced by the corresponding differentiation matrices

$$\frac{\partial\hat{\varphi}}{\partial y} = \boldsymbol{P}_y\hat{\Phi}, \frac{\partial^2\hat{\varphi}}{\partial y^2} = \boldsymbol{P}_{yy}\hat{\Phi} \tag{22}$$

with a fourth-order central difference scheme:

$$\frac{\partial\hat{\varphi}_j}{\partial y} = \frac{\hat{\varphi}_{j-2} - 8\hat{\varphi}_{j-1} + 8\hat{\varphi}_{j+1} - \hat{\varphi}_{j+2}}{12\Delta y}, \tag{23a}$$

$$\frac{\partial^2\hat{\varphi}_j}{\partial y^2} = \frac{-\hat{\varphi}_{j-2} + 16\hat{\varphi}_{j-1} - 30\hat{\varphi}_j + 16\hat{\varphi}_{j+1} - \hat{\varphi}_{j+2}}{12(\Delta y)^2}. \tag{23b}$$

According to Schmid and Henningson [38], to achieve the highest possible accuracy, the mapping

$$y = a\frac{1+\bar{y}}{b-\bar{y}}, \text{with } a = \frac{y_i y_{\max}}{y_{\max} - 2y_i}, b = 1 + \frac{2a}{y_{\max}}, \bar{y} \in [-1, 1] \tag{24}$$

allows for a clustering of one half of grid points to the interval $[0, y_i]$.

Eqs. (16) and (19) are finally reduced to a system of algebraic equations below which can be readily solved by a marching procedure and eigenvalue solver, respectively.

$$\mathcal{L}\hat{\Phi}_{i+1} = \mathcal{R}\hat{\Phi}_{\mathrm{i}}, \tag{25}$$

$$\mathcal{A}\hat{\Phi} = \alpha\mathcal{B}\hat{\Phi}. \tag{26}$$

The matrices $\mathcal{L}$, $\mathcal{R}$ in eq. (25) and $\mathcal{A}$, $\mathcal{B}$ in eq. (26) consist of the matrices elements in eq. (11) and the finite difference operators. In the solution procedure, the base flow quantities are interpolated on the stability solution grid with the cubic spline interpolation. The boundary conditions applied are

$$\hat{u} = \hat{v} = \hat{w} = \hat{T} = 0, \text{at } y = 0, \tag{27}$$

$$\hat{u} = \hat{v} = \hat{w} = \hat{T} = 0, \text{at } y \to \infty. \tag{28}$$

For the eigenvalue problem, $\hat{\Phi}$ is the eigenvector and α the eigenvalue to be solved. The spatial growth of the infinitesimally small disturbances is obtained by solving the above equation with $\mathrm{Im}(\alpha) < 0$. The full spectrum is calculated with the standard QZ method. In the marching method, the growth rate σ is defined with the use of a local scale as:

$$\sigma = \left(-Im(\alpha) + \frac{\partial}{\partial x}\left(\ln \sqrt{E}\right)\right)\sqrt{\frac{x}{x_0}}. \tag{29}$$

Here, $E = \int_0^\infty \left(\hat{u}^2 + \hat{v}^2 + \hat{w}^2\right) dy$ is the disturbance energy, x is the streamwise coordinate of the specified location and x_0 is the streamwise coordinate where the initial disturbances were applied. The other definitions of the growth rate can be found in eqs. (15) and (17) in the review article by Saric [5].

3 Results and discussion

3.1 Algorithm validation

The present algorithm is first tested and verified for the incompressible Görtler instability flows prior to the compressible cases. Though formulated as a compressible flow, the present code should be capable of characterizing the flow at the low speed regime. For the 9 mm wavelength case of Li and Malik [29], the linear and nonlinear development of the Görtler vortices is shown in Figure 2 with nine Fourier modes. The disturbance energy matches well with Li and Malik. A global watch of the nonlinear development of the Görtler vortices is shown in Figure 3.

The feasibility for compressible cases was tested with the first mode of TS wave in the boundary layer of $Ma = 4.5$. The initial disturbances with frequency $\omega = 0.0533$, streamwise wavenumber $\alpha = 0.064$ and amplitude $A = 0.01$ was imposed at $Re_0 = 10471$. The resulting disturbances of the marching analysis agree well with the DNS profiles at $x = 516$ downstream of the starting point [39]. The corresponding disturbances u and T for the Fourier modes (0,0), (1,0) and (2,0)

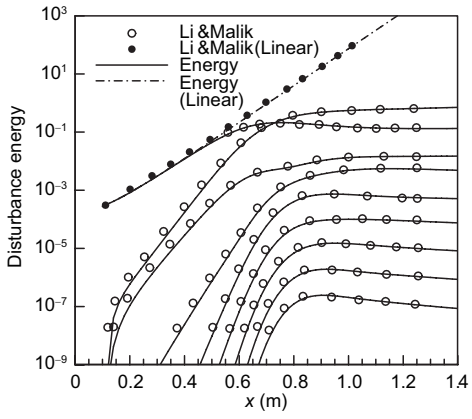

Figure 2 The linear and nonlinear development of disturbance energy of Görtler vortices. The truncated Fourier modes of 0–8 were shown.

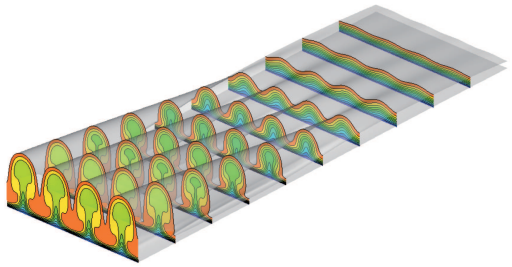

Figure 3 (Color online) The nonlinear development of Görtler vortices characterized by the contours of the streamwise velocity. Ten slices are given here ranging from x =0.1 m to 1.2 m.

are shown in Figure 4. In the above two cases, the marching analysis results were tested to be grid-independent.

With the present local method, the classic neutral curves [36] of (Mode 1 and 2, incompressible flow) and the disturbance profiles [28] are recovered as shown in Figures 5 and 6. Both the neutral curves and the disturbance profiles agree well with the existing results.

In the compressible regime, calculations are performed for the parameters of El-Hady and Verma [40]. The comparisons are shown in Figure 7 for $Ma = 1, 2, \cdots, 5$ with the results of Whang and Zhong [41].

Figure 7 shows a nice convergence with grid density. The influence of the far-field position is also examined here. Comparisons above show that the present work characterizes well the Görtler instability in supersonic and hypersonic flows. As can be seen 400 girds are sufficient for the analysis and will be used in the subsequent calculation considering the efficiency and accuracy. It should be pointed out that higher Ma number calculations need more grids to obtain a high-accuracy result.

3.2 Eigen spectrum and the multiple modes

Since the present work is to study the multiple Görtler modes and their effect on the flow stabilities in the compressible boundary layers, it is important to identify each individual mode in the numerical computation and track down its behavior. The disturbance modes are related to the solutions of the eigenvalue problem. The present mode tracking approach is thus based on the crosschecking of the eigenvectors. For the wall-layer modes (mode W), the primary mode (mode W1) corresponds to the largest eigenvalue solution with one independent Görtler vortex, the secondary mode (mode W2) corresponds to the second largest eigenvalue solution with two independent Görtler vortices. This is usually the case in the incompressible problems. In the compressible boundary layer flows, however, Mach number comes into play a dominant role in addition to the Reynolds and the Görtler numbers, that sequence may be influenced by the trapped-layer mode (mode T). As will be shown later, the crossover of the mode W1 and mode T may indeed take place.

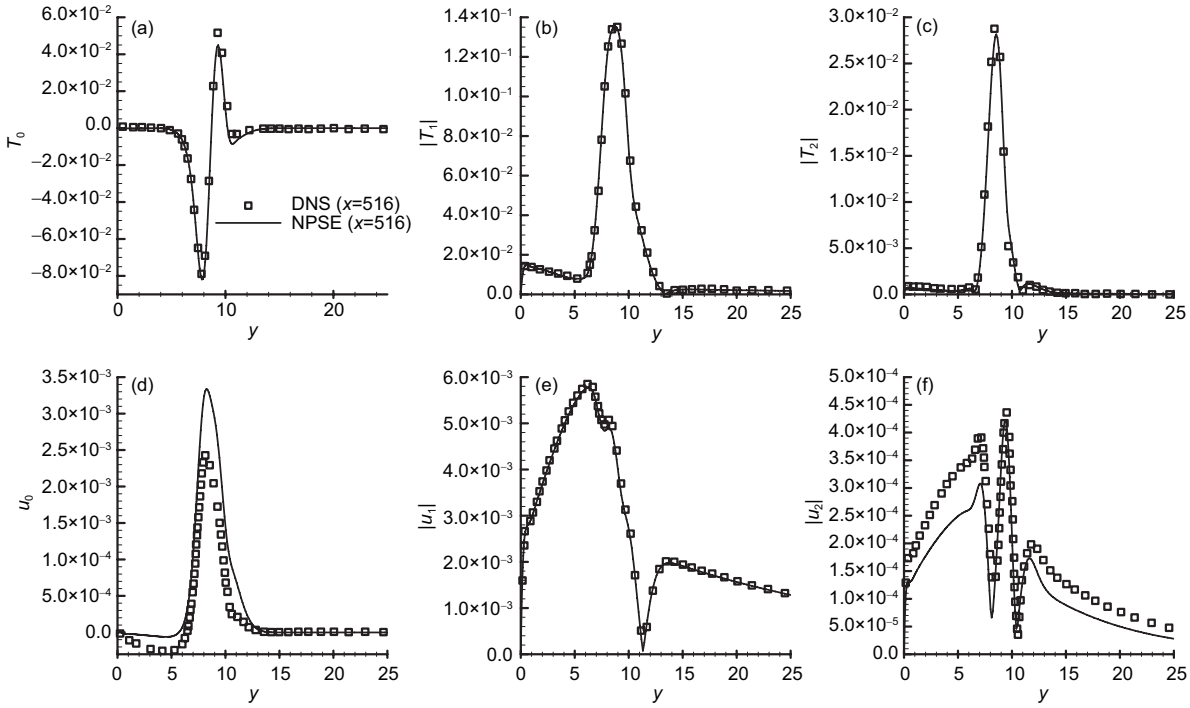

Figure 4 Disturbance profiles (a) $\hat{T}(0,0)$, (b) $|\hat{T}(1,0)|$, (c) $|\hat{T}(2,0)|$, (d) $\hat{u}(0,0)$, (e) $|\hat{u}(1,0)|$ and (f) $|\hat{u}(2,0)|$ at $x = 516$ downstream of the starting point: ——, DNS; □, Marching analysis (NPSE).

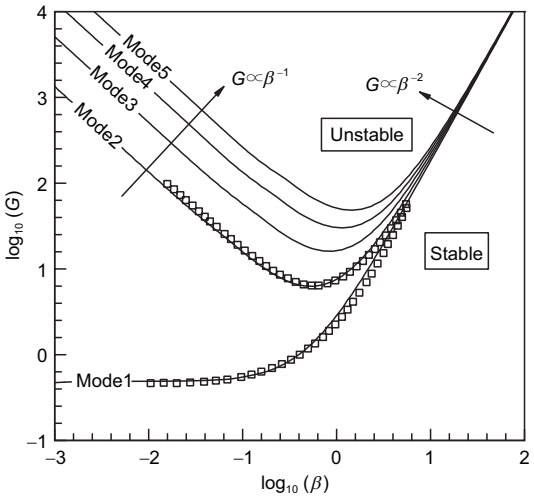

Figure 5 Neutral curve of incompressible Görtler instability for mode 1 – –5 under a very low Mach number of 0.01 and a fixed curvature of 10^{-6}: ——, nonparallel baseflow; □, results given in ref. [36].

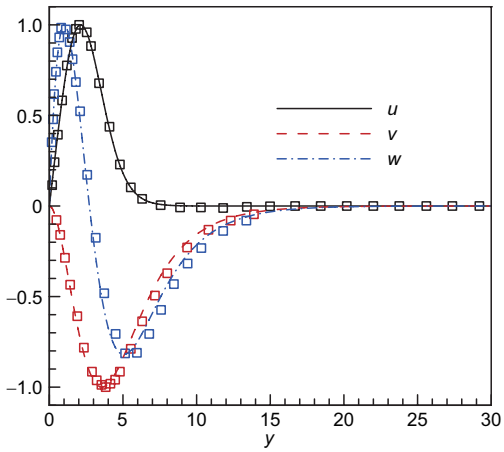

Figure 6 (Color online) Disturbance profiles with the control parameters of Lee and Liu [28] at $x^* = 0.4$ m: ——, current local analysis; □ results given by Lee and Liu [28].

A typical case of the spectrum of the Görtler modes and their corresponding disturbances are shown in Figure 8. The existing seven Görtler modes are circled against other pseudo eigenvalues. All the Görtler eigenvalues are located on the quasi-imaginary-axis, i.e., the wavenumber $Re(\alpha) \approx 0$. This is consistent with the physical phenomenon where no streamwise wave exists. The spatial structures of these modes are presented in Figure 9 in the form of the streamwise perturbation velocity contours. It can be inferred that the most amplified mode is mode T and the other modes are mode W1–W6.

3.3 Mode competition: The local analysis

To define a neutral curve in the G-β map, calculations are carried out with a number of cases. Here, the curvature $k = -10^{-6}$ and Mach number Ma =0.95, 2, 4 and 6 are fixed and each case is characterized with the wavenumber β and the Görtler number G. Below, the contours of the disturbance growth rate for the two most amplified Görtler modes are

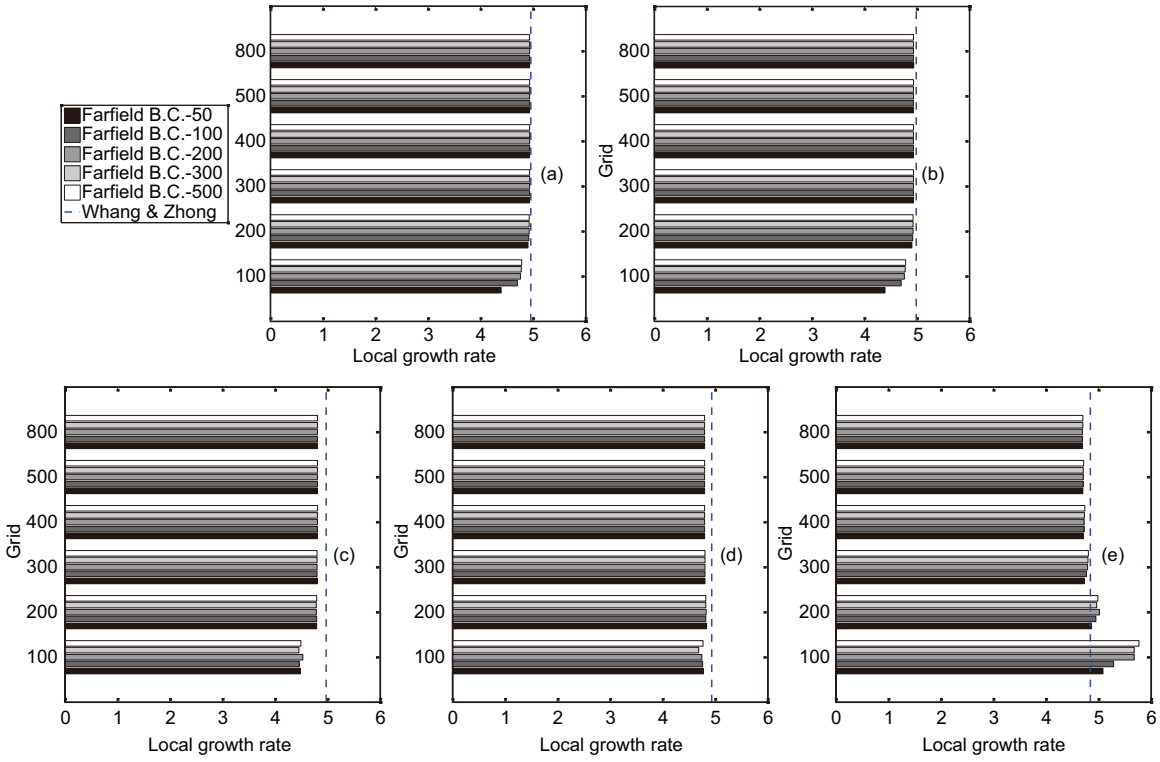

Figure 7 Comparisons of the local growth rate with Whang and Zhong [41] (dashed lines). Far-field boundary conditions are specified at $y_{\max} = 50\delta_0^*$, $100\delta_0^*$, $200\delta_0^*$, $300\delta_0^*$, $500\delta_0^*$, respectively. (a) Ma=1; (b) Ma=2; (c) Ma=3; (d) Ma=4; (e) Ma=5.

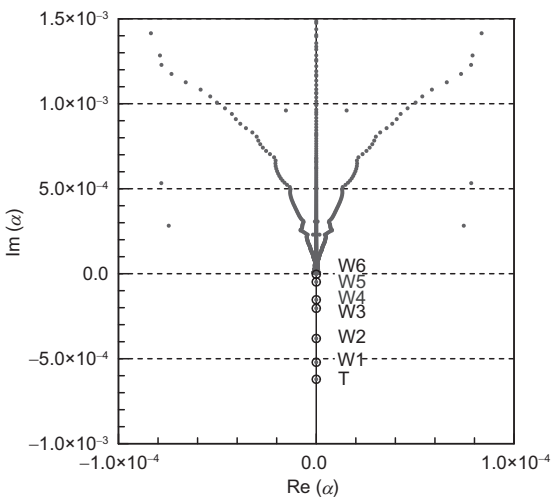

Figure 8 Eigenvalue spectrum of a typical Görtler instability. Ma = 4, $k = -10^{-6}$, β = 1.1514, G = 954.0955.

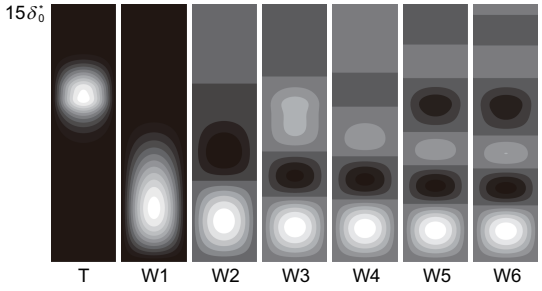

Figure 9 Contours of streamwise velocity perturbation $\hat{u}$ for the most amplified seven Görtler Modes with the same control parameters as in Figure 8.

given in Figure 10. For the cases of Ma =0.95 and 2, the most amplified modes are the mode W1 and W2 described with black and red lines, respectively. While in the Ma =4 and 6 cases, the black lines stand for the mode T and the red lines for the mode W1. The curves with zero growth rates indicate the neutral stability curve. The results were obtained with both quasi-parallel and nonparallel base flows which are denoted with the dashed lines and the solid lines, respectively. The crossover of the contours of the growth rate for the mode T and mode W1 are observed at Ma = 4 and 6 when the Görtler number are sufficiently large. The switch of the dominating modes from the mode T to mode W1 is likely to influence the transition process.

Also, as shown in Figure 11, a typical wavenumber is chosen as β = 0.91. The results obtained with the quasi-parallel base flows are given. The compressibility shows a stabilizing effect as the local growth rate drops with the increase of Ma number. For this specified wavenumber, the initially most amplified mode T is being overtaken by mode W1 when G increases. The crossover points are denoted with the circles. It is interesting to note that this mode crossover takes place at the wavenumbers of the Görtler instability of practical interest.

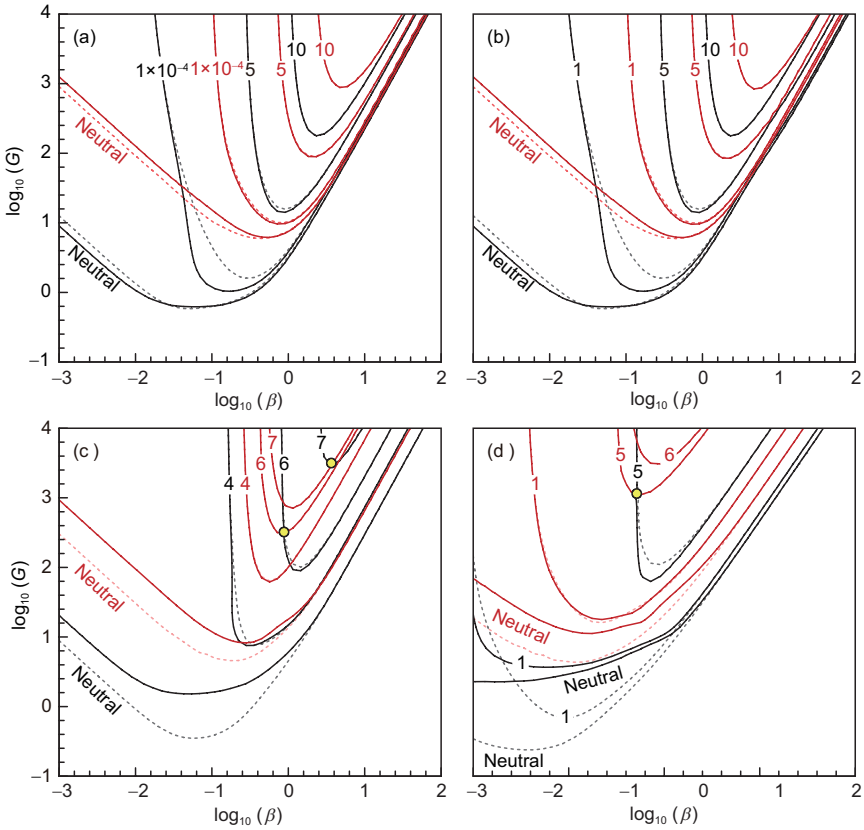

Figure 10 (Color online) Contours of the disturbance local growth rate for the most amplified two modes. Labels in the figure indicate the local growth rate with a multiplier of 10^{-4}: ——, most amplified mode, nonparallel base flow; · · · · · ·, most amplified mode, quasi-parallel base flow; ——, second amplified mode, nonparallel base flow; · · · · · ·, second amplified mode, quasi-parallel base flow. (a) Ma = 0.95; (b) Ma = 2.0; (c) Ma = 4.0; (d) Ma = 6.0.

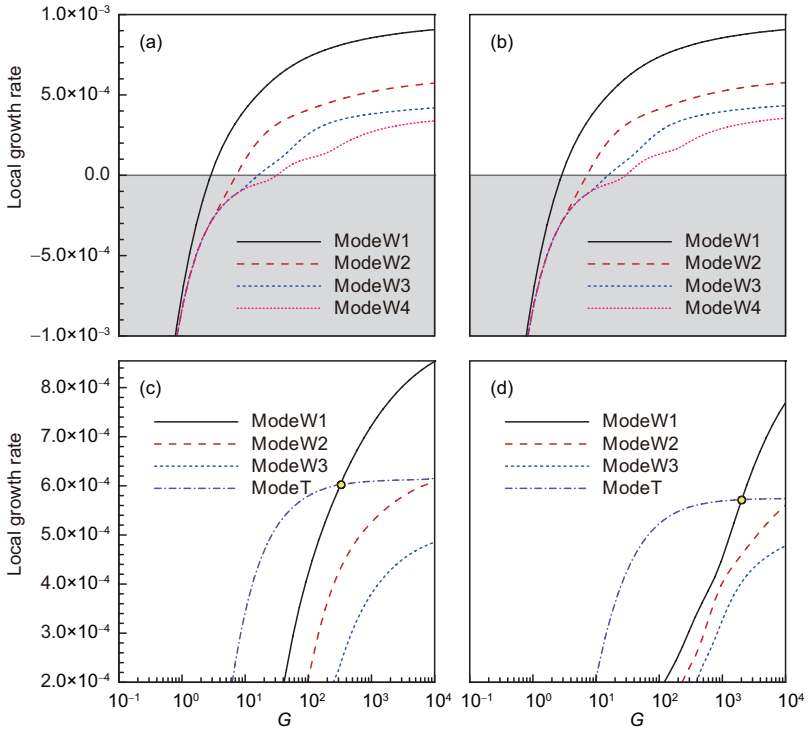

Figure 11 (Color online) Local growth rate of the multiple Görtler modes at β=0.91. (a) Ma = 0.95; (b) Ma = 2.0; (c) Ma = 4.0; (d) Ma = 6.0.

In all the cases including low and high-speed flows with *Ma* ranges from 0.01 to 6, as shown in Figures 5 and 10, the right branch of the neutral curve is free from the influence of the parallel flow assumption. When G is large enough, the nonparallel effects cease to influence the stability behavior wherever the wavenumber is located.

Before the marching analysis is performed, the normal mode solution is presented in a manner with more physical significance. Here, the dimensionless wavelength parameter Λ is used in place of β, as it maintains the physical wavelength when marching downstream. The definition of Λ is

$$\Lambda = \frac{U_\infty^* \lambda^*}{\upsilon_\infty^*} \sqrt{\frac{\lambda^*}{R^*}}. \tag{30}$$

The Greek letter λ stands for the spanwise wave length and R for the radius of curvature. In a "Marching" view, the crossover of the two modes actually takes place for large wavelength instability as shown in Figure 12. The results show little difference between the parallel and nonparallel basic flows. It is interesting and significative that the growth rate drops as G increases for small wavelength cases, e.g., $\Lambda \leqslant 500$. This is essentially different from the incompressible cases [5]. In the incompressible case, the Görtler vortices are likely to fall in the range of $\Lambda \in [10^2, 10^3]$. The increase of G generally helps to increase the growth rate once the disturbance wavelength is located in the amplified region. Nevertheless, in the current *Ma* =4 and 6 case, the maximum amplification occurs within $\Lambda \in [10^2, 10^5]$. This is a much larger range within which the crossover occurs.

Here, we fix some wavelengths for one of the hypersonic cases, e.g., *Ma* =4. Growth rates of different wavelength are plotted in Figure 13. The wavelength parameter ranges from 100.0 to 28117.6. It is obvious that the growth rate of mode T is always larger than mode W1 when G is not too large. This is maintained till the very large wavelength case in Figure 13(b). Crossover of the growth rates takes place for Λ_8 and Λ_9 as shown by the circle mark in the figure.

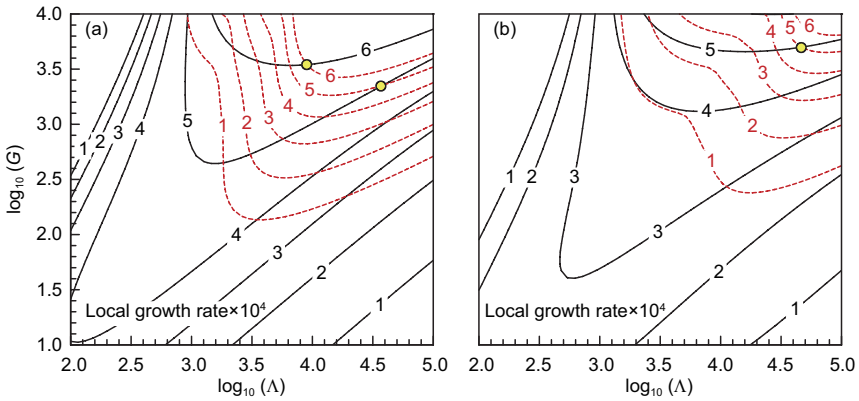

Figure 12 (Color online) Contours of the disturbance local growth rate for the mode T and the mode W1 in the $G - \Lambda$ coordinates. The labels indicate the local growth rate with a magnification of 10^4: ——, mode T; · · · · · ·, mode W1; ○, crossover point.

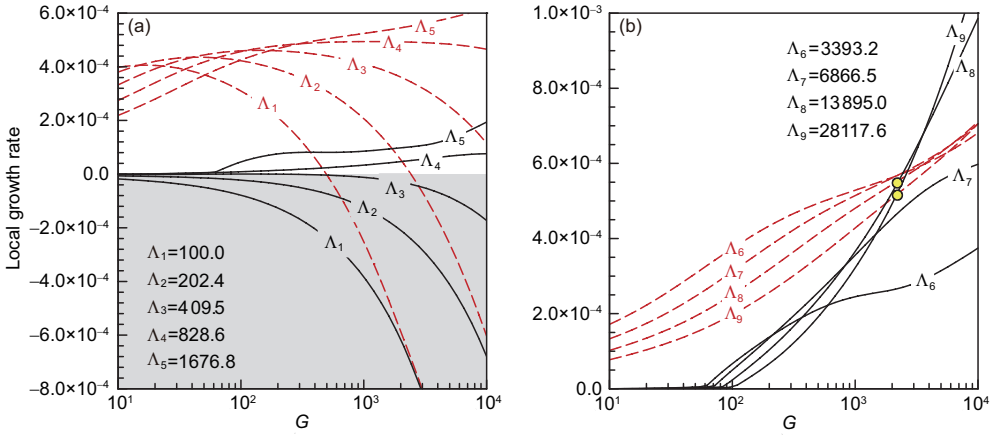

Figure 13 (Color online) Local growth rate of selected wavelengths (*a*) $\Lambda_1 - \Lambda_5$ and (*b*) $\Lambda_6 - \Lambda_9$ for mode T and mode W1 with $G \in [10^1, 10^4]$, *Ma* =4: · · · · · ·, mode T; ——, mode W1; ○, crossover point.

3.4 Mode competition: The marching analysis

The marching analysis is performed for a typical wavelength corresponding to $\Lambda = 16000$. The crossover occurs at $G = 2197.8$ from the local analysis as shown in Figure 14. In fact, four particular regions (Region T, T-W, W-T and W) could be recognized as a prior. The following marching analysis will be performed in five cases covering these regions, respectively.

As described by Bottaro and Luchini [11], the marching and local analysis results agree well for x sufficiently large. Benmalek and Saric [42], in their curvature-variation study, demonstrated that the initial conditions from the local analysis produce no quantitative dependence on the location where they are applied. To minimize the influence of the initial condition, the local profile of the disturbance is applied after the neutral point as the initial condition and the analysis is performed downstream far enough from the influence of the initial condition.

In the view point of the marching analysis, the multi-modes manifest a "single mode". The marching parameters are listed in Table 1. These cases can be selected a posteriori from the marching results.

Case I stands for the region far before the crossover point where the mode T enjoy the definite advantages over the other modes (Region T). As shown in Figure 15(a), though initialized with different modes, the disturbances all prove to be the mode T downstream. The mode W1 undergoes a temporary presence and then a "transformation" to the mode T while it is a short instant for the mode W2 to show up its shape. Evolutions of the disturbance profile $\hat{u}$ are given in the subplot of each figure. The mode W1 has one peak and the disturbances are concentrated in the near wall region. The difference for the mode W2 is the second peak. The mode T also has one peak but the disturbances are detached from the wall. Still before the crossover point, case II shown in Figure 15(b) supports the two modes simultaneously. The growth rates of the two modes become closer. The mode W1 now is able to be maintained in the boundary layer. The mode W2 is "captured" by the mode W1 but finally "transformed" into the mode T (Region T-W). Case III passes through the crossover point in Figure 15(c). In this specific region, the growth rates of the most amplified two modes are nearly equal. As was expected, the two modes can co-exist while the mode W2 "transformed" into the mode W1 downstream which is finally the most amplified (Region T-W). In Figures 15(d) and (e), a similar process was noticed where the mode W1 overtakes the mode T (Region W-T and W).

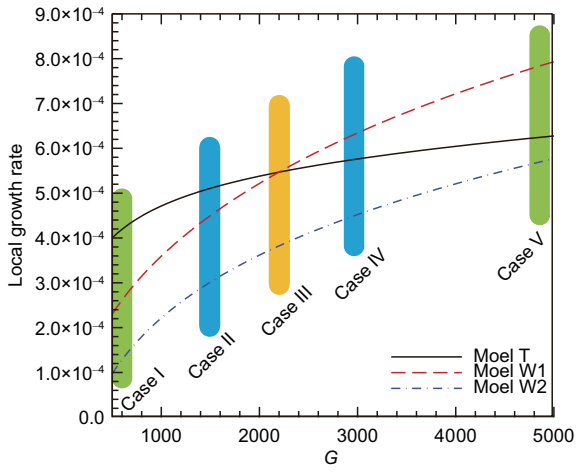

Figure 14 (Color online) Local growth rate of the mode W1, mode W2 and mode T predicted by local analysis. The parameters of the five cases are given in Table 1.

Table 1 Marching parameters of the five cases defined in Figure 14

CASE	Regions	G	Re ($\times 10^6$)	β (local scale)
I	T	500–540	1.357–1.429	0.623–0.656
II	T-W	1500–1540	2.823–2.873	1.300–1.320
III	W-T	2180–2220	3.622–3.666	1.664–1.684
IV	W-T	3000–3040	4.481–4.521	2.058–2.077
V	W	4960–5000	6.266–6.300	2.878–2.893

As a matter of fact, these eigenfunctions of the modes are nonorthogonal. When the initial condition is specified with the eigenfunction of a particular mode for the marching analysis, it also covers the disturbance shape of other modes. Thus, the "transformation" is actually the appearance of the shape (mode T or W1) due to its larger growth rate. Furthermore, the initial condition derived from the normal mode approach in fact projects onto both the W and T modes.

The above marching analysis confirmed the crossover of the mode W1 and the mode T predicted by the local analysis. In the vicinity of the crossover point (Region T-W and W-T), the two modes will both have the chance to be excited and develop downstream. The other mode-shape initialized will finally develop into the shape corresponding to the most amplified mode. Further away from the crossover point, the most amplified mode will be the only survivor in the boundary layer (Region T and W). It should be pointed out that, when the nonlinear effects are considered, the crossover is not obviously influenced [43,44].

As a practical application towards the engineering areas, the RANS modeling can be formulated based on the the linear stability theory [45–47]. Therefore, it is in the Region T-W and W-T discussed above that the multiple modes should be considered.

4 Conclusions

In the compressible boundary layer flows, the competition between the multiple Görtler modes is illustrated with the local and marching analyses. Eigenvalue formulation at the small wave number regime is proved to be inaccurate due to the nonparallel base flow. It can be concluded that the local method is valid either in the large wavenumber region or in the large Görtler number region. The competition between

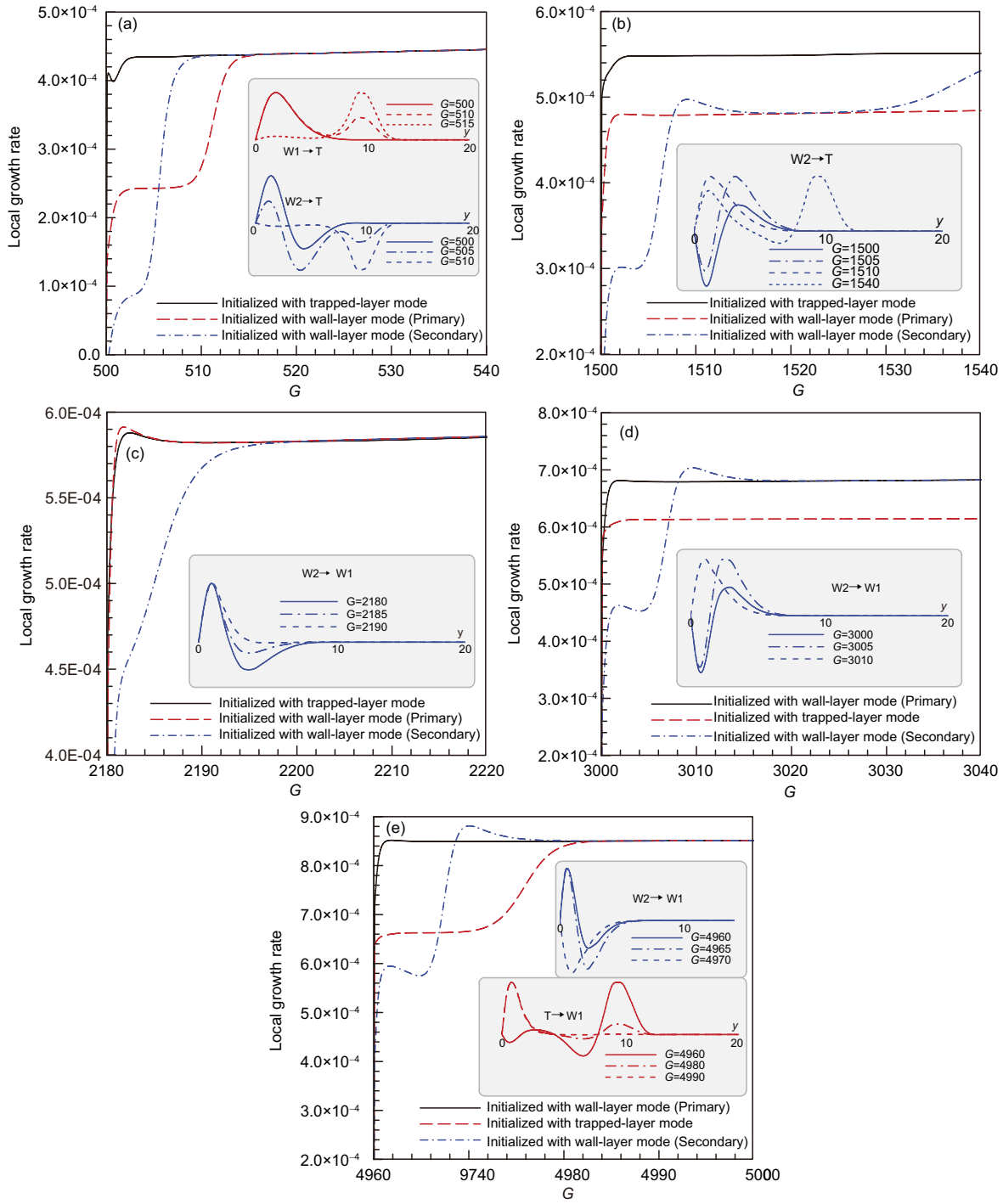

Figure 15 (Color online) Local growth rate of the mode T and the mode W1 and W2 predicted by marching analysis. Evolutions of the disturbance $\hat{u}$ are given in the subplot of each figure. (a) CASE I; (b) CASE II; (c) CASE III; (d) CASE IV; (e) CASE V.

the multiple Görtler modes takes place far beyond the neutral area, i.e., the Görtler number is sufficiently large. Hence, the local analysis is valid.

Investigation into the hypersonic problems brings interesting flow features different to the convectional incompressible flows. The increase in the Görtler number even decreases the growth rate of the trapped-layer mode (mode T) when the wavelength is small. The most amplified wavelength has increased by a remarkable degree of magnitude, i.e, from $\Lambda \in [10^2, 10^3]$ to $\Lambda \in [10^3, 10^5]$. These behaviors are caused by the occurrence of the mode T in hypersonic cases, it does not exist in the incompressible flows as their modal shapes can hardly be formed. Indeed, they are even difficult to be observed experimentally. However, when *Ma* number is in-

creased to a certain value, i.e., $Ma \geqslant 4$, the mode T is the most amplified at an incipient low Görtler number. With the further increase in Görtler number, the mode W1 finally overtakes mode T and becomes the most dangerous mode. The disturbances are, therefore, modulated by different regions (Region T, T-W, W-T and W) when exposed in different Görtler numbers. It is also shown that the compressibility is to insert stabilizing effect on both mode T and mode W.

Appendix

In eq. (11), the matrices $\boldsymbol{\Gamma}$, $\boldsymbol{A}$, $\boldsymbol{B}$, $\boldsymbol{C}$, $\boldsymbol{D}$, $\boldsymbol{H}_{xx}$, $\boldsymbol{H}_{yy}$, $\boldsymbol{H}_{zz}$, $\boldsymbol{H}_{xy}$, $\boldsymbol{H}_{yz}$ and $\boldsymbol{H}_{xz}$ are defined as follows. Only the nonzero elements of these matrices are given. Bearing in mind that the coordinates are defined in Figure 1, the corresponding Lame coefficients are $h_1 = 1 + ky$, $h_2 = 1$, $h_3 = 1$ with k representing the curvature.

Matrix $\boldsymbol{\Gamma}$

$$\boldsymbol{\Gamma}_{11} = 1, \quad \boldsymbol{\Gamma}_{22} = \rho, \quad \boldsymbol{\Gamma}_{33} = \rho, \quad \boldsymbol{\Gamma}_{44} = \rho, \boldsymbol{\Gamma}_{51} = -\frac{\gamma-1}{\gamma}T, \quad \boldsymbol{\Gamma}_{55} = \frac{\rho}{\gamma}$$

Matrix $\boldsymbol{A}$

$$\boldsymbol{A}_{11} = \frac{u}{h_1}, \quad \boldsymbol{A}_{12} = \frac{\rho}{h_1}, \quad \boldsymbol{A}_{21} = \frac{1}{\gamma Ma^2}\frac{1}{h_1}T, \quad \boldsymbol{A}_{22} = \rho\frac{u}{h_1} - \frac{1}{h_1}\frac{4}{3}\frac{\mathrm{d}\mu}{\mathrm{d}T}\frac{\partial T}{\partial x}\frac{1}{Re}\frac{1}{h_1},$$

$$\boldsymbol{A}_{23} = -\frac{1}{h_1}\frac{\mu}{Re}\frac{4}{3}\frac{1}{h_1}\frac{\partial h_1}{\partial y} - \frac{1}{h_1}\frac{\mathrm{d}\mu}{\mathrm{d}T}\frac{\partial T}{\partial y}\frac{1}{Re} - \frac{\mu}{Re}\frac{1}{h_1}\frac{\partial h_1}{\partial y}\frac{1}{h_1},$$

$$\boldsymbol{A}_{25} = -\frac{1}{h_1}\frac{\mathrm{d}\mu}{\mathrm{d}T}\frac{1}{Re}\left(\frac{4}{3}\frac{1}{h_1}\frac{\partial u}{\partial x} + \frac{4}{3}\frac{v}{h_1}\frac{\partial h_1}{\partial y} - \frac{2}{3}\frac{\partial v}{\partial y}\right) + \frac{1}{\gamma Ma^2}\frac{1}{h_1}\rho$$

$$\boldsymbol{A}_{32} = \frac{1}{h_1}\frac{1}{Re}\mu\frac{1}{h_1}\frac{\partial h_1}{\partial y} + \frac{2}{h_1}\frac{\partial h_1}{\partial y}\frac{1}{Re}\mu\frac{1}{h_1} + \frac{2}{3}\frac{1}{Re}\frac{\mathrm{d}\mu}{\mathrm{d}T}\frac{\partial T}{\partial y}\frac{1}{h_1} - \frac{2}{3}\frac{\mu}{Re}\frac{1}{h_1}\frac{1}{h_1}\frac{\partial h_1}{\partial y}$$

$$\boldsymbol{A}_{33} = \rho\frac{u}{h_1} - \frac{1}{h_1}\frac{1}{Re}\frac{\mathrm{d}\mu}{\mathrm{d}T}\frac{\partial T}{\partial x}\frac{1}{h_1}, \quad \boldsymbol{A}_{35} = -\frac{1}{h_1}\frac{1}{Re}\frac{\mathrm{d}\mu}{\mathrm{d}T}\left(\frac{\partial u}{\partial y} + \frac{1}{h_1}\frac{\partial v}{\partial x} - \frac{u}{h_1}\frac{\partial h_1}{\partial y}\right)$$

$$\boldsymbol{A}_{44} = \rho\frac{u}{h_1} - \frac{1}{h_1}\frac{\mathrm{d}\mu}{\mathrm{d}T}\frac{\partial T}{\partial x}\frac{1}{Re}\frac{1}{h_1}, \quad \boldsymbol{A}_{45} = -\frac{1}{h_1}\frac{\mathrm{d}\mu}{\mathrm{d}T}\frac{1}{Re}\frac{1}{h_1}\frac{\partial w}{\partial x}$$

$$\boldsymbol{A}_{51} = -\frac{\gamma-1}{\gamma}T\frac{u}{h_1}, \quad \boldsymbol{A}_{52} = \frac{4}{3}\frac{(\gamma-1)Ma^2}{Re}\mu\left(\frac{1}{h_1}\frac{\partial v}{\partial y} - \frac{2}{h_1}\frac{1}{h_1}\frac{\partial u}{\partial x} - 2\frac{1}{h_1}\frac{v}{h_1}\frac{\partial h_1}{\partial y}\right)$$

$$\boldsymbol{A}_{53} = -2\frac{(\gamma-1)Ma^2}{Re}\mu\left(\frac{1}{h_1}\frac{1}{h_1}\frac{\partial v}{\partial x} + \frac{1}{h_1}\frac{\partial u}{\partial y} - \frac{1}{h_1}\frac{1}{h_1}u\frac{\partial h_1}{\partial y}\right)$$

$$\boldsymbol{A}_{54} = -2\frac{(\gamma-1)Ma^2}{Re}\mu\frac{1}{h_1}\frac{1}{h_1}\frac{\partial w}{\partial x}, \quad \boldsymbol{A}_{55} = \frac{\rho}{\gamma}\frac{u}{h_1} - \frac{2}{RePr}\frac{1}{h_1}\frac{1}{h_1}\frac{\mathrm{d}\kappa}{\mathrm{d}T}\frac{\partial T}{\partial x}$$

Matrix $\boldsymbol{B}$

$$\boldsymbol{B}_{11} = v, \quad \boldsymbol{B}_{13} = \rho, \quad \boldsymbol{B}_{22} = \rho v - \frac{\mathrm{d}\mu}{\mathrm{d}T}\frac{\partial T}{\partial y}\frac{1}{Re} - \frac{\mu}{Re}\frac{1}{h_1}\frac{\partial h_1}{\partial y}, \quad \boldsymbol{B}_{23} = \frac{2}{3}\frac{\mathrm{d}\mu}{\mathrm{d}T}\frac{\partial T}{\partial x}\frac{1}{Re}\frac{1}{h_1}$$

$$\boldsymbol{B}_{25} = -\frac{1}{h_1}\frac{\mathrm{d}\mu}{\mathrm{d}T}\frac{1}{Re}\left(h_1\frac{\partial u}{\partial y} + \frac{\partial v}{\partial x} - u\frac{\partial h_1}{\partial y}\right), \quad \boldsymbol{B}_{31} = \frac{T}{\gamma Ma^2}, \quad \boldsymbol{B}_{32} = -\frac{1}{h_1}\frac{1}{Re}\frac{\mathrm{d}\mu}{\mathrm{d}T}\frac{\partial T}{\partial x},$$

$$\boldsymbol{B}_{33} = \rho v - \frac{2}{h_1}\frac{\partial h_1}{\partial y}\frac{1}{Re}\mu - \frac{4}{3}\frac{1}{Re}\frac{\mathrm{d}\mu}{\mathrm{d}T}\frac{\partial T}{\partial y} + \frac{2}{3}\frac{\mu}{Re}\frac{1}{h_1}\frac{\partial h_1}{\partial y}, \quad \boldsymbol{B}_{35} = \frac{\rho}{\gamma Ma^2} + \frac{1}{Re}\frac{\mathrm{d}\mu}{\mathrm{d}T}\left(\frac{2}{3}\frac{1}{h_1}\frac{\partial u}{\partial x} + \frac{2}{3}\frac{v}{h_1}\frac{\partial h_1}{\partial y} - \frac{4}{3}\frac{\partial v}{\partial y}\right)$$

$$\boldsymbol{B}_{44} = \rho v - \frac{1}{h_1}\frac{\partial h_1}{\partial y}\frac{1}{Re}\mu - \frac{1}{Re}\frac{\mathrm{d}\mu}{\mathrm{d}T}\frac{\partial T}{\partial y}, \quad \boldsymbol{B}_{45} = -\frac{1}{Re}\frac{\mathrm{d}\mu}{\mathrm{d}T}\frac{\partial w}{\partial y}, \quad \boldsymbol{B}_{51} = -\frac{\gamma-1}{\gamma}Tv$$

$$\boldsymbol{B}_{52} = -2\frac{(\gamma-1)Ma^2}{Re}\mu\left(\frac{\partial u}{\partial y} + \frac{1}{h_1}\frac{\partial v}{\partial x} - \frac{1}{h_1}u\frac{\partial h_1}{\partial y}\right), \quad \boldsymbol{B}_{53} = \frac{4}{3}\frac{(\gamma-1)Ma^2}{Re}\mu\left(-2\frac{\partial v}{\partial y} + \frac{1}{h_1}\frac{\partial u}{\partial x} + \frac{v}{h_1}\frac{\partial h_1}{\partial y}\right)$$

$$\boldsymbol{B}_{54} = -2\frac{(\gamma-1)Ma^2}{Re}\mu\frac{\partial w}{\partial y}, \quad \boldsymbol{B}_{55} = \frac{1}{\gamma}\rho v - \frac{2}{RePr}\frac{\mathrm{d}\kappa}{\mathrm{d}T}\frac{\partial T}{\partial y} - \frac{1}{RePr}\frac{1}{h_1}\frac{\partial h_1}{\partial y}\kappa$$

Matrix $\boldsymbol{C}$

$$\boldsymbol{C}_{11}=w,\quad \boldsymbol{C}_{14}=\rho,\quad \boldsymbol{C}_{22}=\rho w,\quad \boldsymbol{C}_{24}=\frac{2}{3}\frac{1}{h_1}\frac{\mathrm{d}\mu}{\mathrm{d}T}\frac{\partial T}{\partial x}\frac{1}{Re},\quad \boldsymbol{C}_{25}=-\frac{1}{h_1}\frac{\mathrm{d}\mu}{\mathrm{d}T}\frac{1}{Re}\frac{\partial w}{\partial x}$$

$$\boldsymbol{C}_{33}=\rho w,\quad \boldsymbol{C}_{34}=\frac{2}{3}\frac{1}{Re}\frac{\mathrm{d}\mu}{\mathrm{d}T}\frac{\partial T}{\partial y},\quad \boldsymbol{C}_{35}=-\frac{\mathrm{d}\mu}{\mathrm{d}T}\frac{1}{Re}\frac{\partial w}{\partial y},\quad \boldsymbol{C}_{41}=\frac{T}{\gamma Ma^2},\quad \boldsymbol{C}_{42}=-\frac{1}{h_1}\frac{\mathrm{d}\mu}{\mathrm{d}T}\frac{\partial T}{\partial x}\frac{1}{Re}$$

$$\boldsymbol{C}_{43}=\frac{2}{3}\mu\frac{1}{Re}\frac{1}{h_1}\frac{\partial h_1}{\partial y}-\frac{1}{Re}\frac{\mathrm{d}\mu}{\mathrm{d}T}\frac{\partial T}{\partial y}-\frac{1}{h_1}\frac{\partial h_1}{\partial y}\frac{1}{Re}\mu,\quad \boldsymbol{C}_{44}=\rho w$$

$$\boldsymbol{C}_{45}=\frac{1}{\gamma Ma^2}\rho-\frac{\partial\mu}{\partial T}\left(-\frac{2}{3}\frac{1}{Re}\frac{1}{h_1}\frac{\partial u}{\partial x}-\frac{2}{3}\frac{1}{Re}\frac{v}{h_1}\frac{\partial h_1}{\partial y}-\frac{2}{3}\frac{1}{Re}\frac{\partial v}{\partial y}\right),\quad \boldsymbol{C}_{51}=-\frac{\gamma-1}{\gamma}Tw$$

$$\boldsymbol{C}_{52}=-2\frac{(\gamma-1)\,Ma^2}{Re}\mu\frac{1}{h_1}\frac{\partial w}{\partial x},\quad \boldsymbol{C}_{53}=-2\frac{(\gamma-1)\,Ma^2}{Re}\mu\frac{\partial w}{\partial y}$$

$$\boldsymbol{C}_{54}=\frac{4}{3}\frac{(\gamma-1)\,Ma^2}{Re}\mu\left(\frac{1}{h_1}\frac{\partial u}{\partial x}+\frac{v}{h_1}\frac{\partial h_1}{\partial y}+\frac{\partial v}{\partial y}\right),\quad \boldsymbol{C}_{55}=\frac{\rho w}{\gamma}$$

Matrix $\boldsymbol{D}$

$$\boldsymbol{D}_{11}=\frac{1}{h_1}\frac{\partial u}{\partial x}+\frac{\partial v}{\partial y}+\frac{\partial h_1}{\partial y}\frac{v}{h_1},\quad \boldsymbol{D}_{12}=\frac{1}{h_1}\frac{\partial\rho}{\partial x},\quad \boldsymbol{D}_{13}=\frac{\partial\rho}{\partial y}+\frac{\partial h_1}{\partial y}\frac{\rho}{h_1}$$

$$\boldsymbol{D}_{21}=\frac{u}{h_1}\frac{\partial u}{\partial x}+v\frac{\partial u}{\partial y}+\frac{uv}{h_1}\frac{\partial h_1}{\partial y}+\frac{1}{\gamma Ma^2}\frac{1}{h_1}\frac{\partial T}{\partial x}$$

$$\boldsymbol{D}_{22}=\frac{\rho}{h_1}\frac{\partial u}{\partial x}+\frac{\rho v}{h_1}\frac{\partial h_1}{\partial y}+\frac{1}{h_1}\frac{\mathrm{d}\mu}{\mathrm{d}T}\frac{\partial T}{\partial y}\frac{1}{Re}\frac{\partial h_1}{\partial y}+\frac{\mu}{Re}\frac{1}{h_1}\frac{\partial h_1}{\partial y}\left(\frac{1}{h_1}\frac{\partial h_1}{\partial y}\right)$$

$$\boldsymbol{D}_{23}=\rho\frac{\partial u}{\partial y}+\rho\frac{u}{h_1}\frac{\partial h_1}{\partial y}-\frac{1}{h_1}\frac{\mathrm{d}\mu}{\mathrm{d}T}\frac{\partial T}{\partial x}\frac{1}{Re}\left(\frac{4}{3}\frac{1}{h_1}\frac{\partial h_1}{\partial y}\right)$$

$$\begin{aligned}\boldsymbol{D}_{25}=&-\frac{1}{h_1}\frac{\mathrm{d}^2\mu}{\mathrm{d}T^2}\frac{\partial T}{\partial x}\frac{1}{Re}\left(\frac{4}{3}\frac{1}{h_1}\frac{\partial u}{\partial x}+\frac{4}{3}\frac{v}{h_1}\frac{\partial h_1}{\partial y}-\frac{2}{3}\frac{\partial v}{\partial y}\right)-\frac{1}{h_1}\frac{\mathrm{d}^2\mu}{\mathrm{d}T^2}\frac{\partial T}{\partial y}\frac{1}{Re}\left(h_1\frac{\partial u}{\partial y}+\frac{\partial v}{\partial x}-u\frac{\partial h_1}{\partial y}\right)\\&-\frac{\mathrm{d}\mu}{\mathrm{d}T}\frac{1}{Re}\frac{1}{h_1}\frac{\partial h_1}{\partial y}\left(\frac{\partial u}{\partial y}+\frac{1}{h_1}\frac{\partial v}{\partial x}-\frac{u}{h_1}\frac{\partial h_1}{\partial y}\right)-\frac{1}{h_1}\frac{\mathrm{d}\mu}{\mathrm{d}T}\frac{1}{Re}\left(h_1\frac{\partial^2 u}{\partial y^2}+\frac{\partial^2 v}{\partial x\partial y}\right)+\frac{1}{\gamma Ma^2}\frac{1}{h_1}\frac{\partial\rho}{\partial x}\\&-\frac{1}{h_1}\frac{\mathrm{d}\mu}{\mathrm{d}T}\frac{1}{Re}\left(\frac{4}{3}\frac{1}{h_1}\frac{\partial^2 u}{\partial x^2}+\frac{4}{3}\frac{\partial v}{\partial x}\frac{1}{h_1}\frac{\partial h_1}{\partial y}-\frac{2}{3}\frac{\partial^2 v}{\partial x\partial y}\right)\end{aligned}$$

$$\boldsymbol{D}_{31}=\frac{u}{h_1}\frac{\partial v}{\partial x}+v\frac{\partial v}{\partial y}-\frac{uu}{h_1}\frac{\partial h_1}{\partial y}+\frac{1}{\gamma Ma^2}\frac{\partial T}{\partial y},\quad \boldsymbol{D}_{32}=\frac{\rho}{h_1}\frac{\partial v}{\partial x}-2\rho\frac{u}{h_1}\frac{\partial h_1}{\partial y}+\frac{1}{h_1}\frac{1}{Re}\frac{\mathrm{d}\mu}{\mathrm{d}T}\frac{\partial T}{\partial x}\frac{1}{h_1}\frac{\partial h_1}{\partial y}$$

$$\boldsymbol{D}_{33}=\rho\frac{\partial v}{\partial y}+\frac{2}{h_1}\frac{\partial h_1}{\partial y}\frac{1}{Re}\mu\frac{1}{h_1}\frac{\partial h_1}{\partial y}+\frac{2}{3}\frac{1}{Re}\frac{\mathrm{d}\mu}{\mathrm{d}T}\frac{\partial T}{\partial y}\frac{1}{h_1}\frac{\partial h_1}{\partial y}-\frac{2}{3}\frac{1}{Re}\mu\frac{1}{h_1}\frac{1}{h_1}\frac{\partial h_1}{\partial y}\frac{\partial h_1}{\partial y}$$

$$\begin{aligned}\boldsymbol{D}_{35}=&\frac{1}{\gamma Ma^2}\frac{\partial\rho}{\partial y}-\frac{1}{h_1}\frac{1}{Re}\frac{\mathrm{d}^2\mu}{\mathrm{d}T^2}\frac{\partial T}{\partial x}\left(\frac{\partial u}{\partial y}+\frac{1}{h_1}\frac{\partial v}{\partial x}-\frac{u}{h_1}\frac{\partial h_1}{\partial y}\right)-\frac{1}{h_1}\frac{1}{Re}\frac{\mathrm{d}\mu}{\mathrm{d}T}\left(\frac{\partial^2 u}{\partial x\partial y}+\frac{1}{h_1}\frac{\partial^2 v}{\partial x^2}-\frac{\partial u}{\partial x}\frac{1}{h_1}\frac{\partial h_1}{\partial y}\right)\\&-\frac{2}{h_1}\frac{\partial h_1}{\partial y}\frac{1}{Re}\frac{\mathrm{d}\mu}{\mathrm{d}T}\left(\frac{\partial v}{\partial y}-\frac{1}{h_1}\frac{\partial u}{\partial x}-\frac{v}{h_1}\frac{\partial h_1}{\partial y}\right)+\frac{1}{Re}\frac{\mathrm{d}^2\mu}{\mathrm{d}T^2}\frac{\partial T}{\partial y}\left(\frac{2}{3}\frac{1}{h_1}\frac{\partial u}{\partial x}+\frac{2}{3}\frac{v}{h_1}\frac{\partial h_1}{\partial y}-\frac{4}{3}\frac{\partial v}{\partial y}\right)\\&-\frac{1}{Re}\frac{\mathrm{d}\mu}{\mathrm{d}T}\left(-\frac{2}{3}\frac{1}{h_1}\frac{\partial^2 u}{\partial x\partial y}-\frac{2}{3}\frac{1}{h_1}\frac{\partial v}{\partial y}\frac{\partial h_1}{\partial y}+\frac{4}{3}\frac{\partial^2 v}{\partial y^2}+\frac{2}{3}\frac{1}{h_1}\frac{1}{h_1}\frac{\partial h_1}{\partial y}\frac{\partial u}{\partial x}+\frac{2}{3}\frac{1}{h_1}\frac{v}{h_1}\frac{\partial h_1}{\partial y}\frac{\partial h_1}{\partial y}\right)\end{aligned}$$

$$\boldsymbol{D}_{41}=\frac{u}{h_1}\frac{\partial w}{\partial x}+v\frac{\partial w}{\partial y},\quad \boldsymbol{D}_{42}=\rho\frac{1}{h_1}\frac{\partial w}{\partial x},\quad \boldsymbol{D}_{43}=\rho\frac{\partial w}{\partial y},$$

$$\boldsymbol{D}_{45}=-\frac{1}{h_1}\frac{\mathrm{d}^2\mu}{\mathrm{d}T^2}\frac{\partial T}{\partial x}\frac{1}{Re}\frac{1}{h_1}\frac{\partial w}{\partial x}-\frac{1}{h_1}\frac{\mathrm{d}\mu}{\mathrm{d}T}\frac{1}{Re}\frac{1}{h_1}\frac{\partial^2 w}{\partial x^2}-\frac{1}{h_1}\frac{\partial h_1}{\partial y}\frac{1}{Re}\frac{\partial\mu}{\partial T}\frac{\partial w}{\partial y}-\frac{1}{Re}\frac{d^2\mu}{\mathrm{d}T^2}\frac{\partial T}{\partial y}\frac{\partial w}{\partial y}-\frac{1}{Re}\frac{\mathrm{d}\mu}{\mathrm{d}T}\frac{\partial^2 w}{\partial y^2}$$

$$\boldsymbol{D}_{51}=\frac{u}{h_1}\frac{\partial T}{\partial x}+v\frac{\partial T}{\partial y}-\frac{\gamma-1}{\gamma}\frac{u}{h_1}\frac{\partial T}{\partial x}-\frac{\gamma-1}{\gamma}v\frac{\partial T}{\partial y}$$

$$\boldsymbol{D}_{52}=\frac{\rho}{h_1}\frac{\partial T}{\partial x}-\frac{\gamma-1}{\gamma}\left(\frac{1}{h_1}\rho\frac{\partial T}{\partial x}+\frac{1}{h_1}T\frac{\partial \rho}{\partial x}\right)+2\frac{(\gamma-1)Ma^2}{Re}\mu\left(-\frac{1}{h_1}\frac{\partial h_1}{\partial y}\frac{1}{h_1}u\frac{\partial h_1}{\partial y}+\frac{1}{h_1}\frac{\partial v}{\partial x}\frac{1}{h_1}\frac{\partial h_1}{\partial y}+\frac{\partial u}{\partial y}\frac{1}{h_1}\frac{\partial h_1}{\partial y}\right)$$

$$\boldsymbol{D}_{53}=\rho\frac{\partial T}{\partial y}-\frac{\gamma-1}{\gamma}\left(\rho\frac{\partial T}{\partial y}+T\frac{\partial \rho}{\partial y}\right)-2\frac{(\gamma-1)Ma^2}{Re}\mu\left(\begin{array}{l}+\frac{4}{3}\frac{1}{h_1}\frac{\partial u}{\partial x}\frac{1}{h_1}\frac{\partial h_1}{\partial y}+\frac{4}{3}\frac{1}{h_1}\frac{v}{h_1}\frac{\partial h_1}{\partial y}\frac{\partial h_1}{\partial y}\\-\frac{2}{3}\frac{1}{h_1}\frac{\partial h_1}{\partial y}\frac{\partial v}{\partial y}\end{array}\right)$$

$$\boldsymbol{D}_{55}=-\frac{\gamma-1}{\gamma}\frac{u}{h_1}\frac{\partial \rho}{\partial x}-\frac{\gamma-1}{\gamma}v\frac{\partial \rho}{\partial y}-\frac{1}{RePr}\frac{1}{h_1}\frac{1}{h_1}\frac{d^2\kappa}{\mathrm{d}T^2}\frac{\partial T}{\partial x}\frac{\partial T}{\partial x}-\frac{1}{RePr}\frac{1}{h_1}\frac{1}{h_1}\frac{\mathrm{d}\kappa}{\mathrm{d}T}\frac{\partial^2 T}{\partial x^2}-\frac{1}{RePr}\frac{d^2\kappa}{\mathrm{d}T^2}\frac{\partial T}{\partial y}\frac{\partial T}{\partial y}$$
$$-\frac{1}{RePr}\frac{1}{h_1}\frac{\partial h_1}{\partial y}\frac{\mathrm{d}\kappa}{\mathrm{d}T}\frac{\partial T}{\partial y}-\frac{1}{RePr}\frac{\mathrm{d}\kappa}{\mathrm{d}T}\frac{\partial^2 T}{\partial y^2}$$
$$-\frac{(\gamma-1)Ma^2}{Re}\frac{\mathrm{d}\mu}{\mathrm{d}T}\left[\begin{array}{l}\frac{4}{3}\left(\frac{1}{h_1}\frac{\partial u}{\partial x}+\frac{v}{h_1}\frac{\partial h_1}{\partial y}\right)\left(\frac{1}{h_1}\frac{\partial u}{\partial x}+\frac{v}{h_1}\frac{\partial h_1}{\partial y}\right)+\frac{\partial w}{\partial y}\frac{\partial w}{\partial y}+\frac{4}{3}\frac{\partial v}{\partial y}\frac{\partial v}{\partial y}\\+\frac{1}{h_1}\frac{\partial w}{\partial x}\frac{1}{h_1}\frac{\partial w}{\partial x}-\frac{4}{3}\left(\frac{1}{h_1}\frac{\partial u}{\partial x}+\frac{v}{h_1}\frac{\partial h_1}{\partial y}\right)\left(\frac{\partial v}{\partial y}\right)\\+\left(\frac{1}{h_1}\frac{\partial v}{\partial x}+\frac{\partial u}{\partial y}-\frac{1}{h_1}u\frac{\partial h_1}{\partial y}\right)\left(\frac{1}{h_1}\frac{\partial v}{\partial x}+\frac{\partial u}{\partial y}-\frac{1}{h_1}u\frac{\partial h_1}{\partial y}\right)\end{array}\right]$$

Matrix $\boldsymbol{H}_{xx},\boldsymbol{H}_{xy},\boldsymbol{H}_{xz},\boldsymbol{H}_{yy},\boldsymbol{H}_{yz},\boldsymbol{H}_{zz}$

$$\boldsymbol{H}_{xx22}=\frac{4}{3}\frac{1}{h_1}\frac{1}{h_1}\frac{\mu}{Re},\quad \boldsymbol{H}_{xx33}=\frac{1}{h_1}\frac{1}{h_1}\frac{\mu}{Re},\quad \boldsymbol{H}_{xx44}=\frac{1}{h_1}\frac{1}{h_1}\frac{\mu}{Re},\quad \boldsymbol{H}_{xx55}=\frac{1}{RePr}\frac{1}{h_1}\frac{1}{h_1}\kappa$$
$$\boldsymbol{H}_{xy23}=\frac{1}{3}\frac{1}{h_1}\frac{\mu}{Re},\quad \boldsymbol{H}_{xy32}=\frac{1}{3}\frac{1}{h_1}\frac{\mu}{Re}\quad \boldsymbol{H}_{xz24}=\frac{1}{3}\frac{1}{h_1}\frac{\mu}{Re},\quad \boldsymbol{H}_{xz42}=\frac{1}{3}\frac{1}{h_1}\frac{\mu}{Re}$$
$$\boldsymbol{H}_{yy22}=\frac{\mu}{Re},\quad \boldsymbol{H}_{yy33}=\frac{4}{3}\frac{\mu}{Re},\quad \boldsymbol{H}_{yy44}=\frac{\mu}{Re},\quad \boldsymbol{H}_{yy55}=\frac{\kappa}{RePr}\quad \boldsymbol{H}_{yz34}=\frac{1}{3}\frac{\mu}{Re},$$
$$\boldsymbol{H}_{yz43}=\frac{1}{3}\frac{\mu}{Re}\quad \boldsymbol{H}_{zz22}=\frac{\mu}{Re},\quad \boldsymbol{H}_{zz33}=\frac{\mu}{Re},\quad \boldsymbol{H}_{zz44}=\frac{4}{3}\frac{\mu}{Re},\quad \boldsymbol{H}_{zz55}=\frac{\kappa}{RePr}$$

This work was supported by the National Natural Science Foundation of China (Grant Nos. 10932005 and 11202115).

1 Görtler H. On the three-dimensional instability of laminar boundary layers on concave walls. NACA TM 1375, 1954; translated from "Über eine dreidimensionale Instabilität laminarer Grenzschichten an konkaven Wänden. Des. D. Wiss. Göttingen, Nachr 1940, 1(2)."
2 Herbert T. On the stability of the boundary layer along a concave wall. Archiwum Mechaniki Stosowanej, 1976, 28: 1039–1055
3 Hall P. Görtler vortices in growing boundary-layers: The leading-edge receptivity problem, linear growth and the nonlinear breakdown stage. Mathematika, 1990, 37(2): 151–189
4 Floryan J M. On the Görtler instability of boundary layers. Prog Aerosp Sci, 1991, 28(3): 235–271
5 Saric W S. Görtler vortices. Annu Rev Fluid Mech, 1994, 26: 379–409
6 Floryan J M, Saric W S. Stability of Görtler vortices in boundary layers. AIAA J, 1982, 20(3): 316–324
7 Floryan J M, Saric W S. Wavelength selection and growth of Görtler vortices. AIAA J, 1984, 22(11): 1529–1538
8 Hall P. Taylor-Görtler vortices in fully developed or boundary-layer flows: linear theory. J Fluid Mech, 1982, 124: 475–494
9 Hall P. The linear development of Görtler vortices in growing boundary layers. J Fluid Mech, 1983, 130: 41–58
10 Day H P, Herbert T, Saric W S. Comparing local and marching analysis of Görtler instability. AIAA J, 1990, 28(6): 1010–1015
11 Bottaro A, Luchini P. Görtler vortices: Are they amenable to local eigenvalue analysis? Eur J Mech-B/Fluids, 1999, 18(1): 47–65
12 Goulpié P, Klingmann B G B, Bottaro A. Görtler vortices in boundary layers with streamwise pressure gradient: Linear theory. Phys Fluids, 1996, 8(2): 451–459
13 Wu X, Zhao D, Luo J. Excitation of steady and unsteady Görtler vortices by free-stream vortical disturbances. J Fluid Mech, 2011, 682: 66–100
14 Fedorov A. Transition and stability of high-speed boundary layers. Annu Rev Fluid Mech, 2011, 43: 79–95
15 Zhong X, Wang X. Direct numerical simulation on the receptivity, instability, and transition of hypersonic boundary layers. Annu Rev Fluid Mech, 2012, 44: 527–561
16 Fu Y, Hall P. Crossflow effects on the growth rate of inviscid Görtler vortices in a hypersonic boundary layer. J Fluid Mech, 1994, 276: 343–367
17 Dando A H, Seddougui S O. The compressible Görtler problem in two-dimensional boundary layers. IMA J Appl Math, 1993, 51(1): 27–67
18 Li F, Choudhari M, Chang C, et al. Development and breakdown of Görtler vortices in high speed boundary layers. AIAA Paper, 2010, AIAA- 2010-0705
19 Hall P, Fu Y. On the Görtler vortex instability mechanism at hypersonic speeds. Theoretical and Computational Fluid Dyn, 1989, 1(3): 125–134
20 Fu Y, Hall P. Effects of Görtler vortices, wall cooling and gas dissociation

on the rayleigh instability in a hypersonic boundary layer. J Fluid Mech, 1993, 247: 503–525
21 Hall P, Malik M. The growth of Görtler vortices in compressible boundary layers. J Eng Math, 1989, 23: 239–251
22 Spall R, Malik M. Goertler vortices in supersonic and hypersonic boundary layers. Phys Fluids A Fluid Dyn, 1989, 1(11): 1822–1835
23 Whang C, Zhong X. Receptivity of Görtler vortices in hypersonic boundary layers. AIAA Paper, 2002, AIAA-2002-0151
24 Whang C, Zhong X. Leading edge receptivity of Görtler vortices in a mach 15 flow over a blunt wedge. AIAA Paper, 2003, AIAA-2003-0790
25 Swearingen J D, Blackwelder R F. The growth and breakdown of streamwise vortices in the presence of a wall. J Fluid Mech, 1987, 182: 255–290
26 Hall P. The nonlinear development of Görtler vortices in growing boundary layers. J Fluid Mech, 1988, 193: 243–266
27 Sabry A S, Liu J T C. Longitudinal vorticity elements in boundary layers: nonlinear development from initial Görtler vortices as a prototype problem. J Fluid Mech, 1991, 231: 615–663
28 Lee K, Liu J T C. On the growth of mushroomlike structures in nonlinear spatially developing Goertler vortex flow. Phys Fluids A Fluid Dyn, 1992, 4(1): 95–103
29 Li F, Malik M R. Fundamental and subharmonic secondary instabilities of Görtler vortices. J Fluid Mech, 1995, 297: 77–100
30 Tandiono T, Winoto S H, Shah D A. Spanwise velocity component in nonlinear region of Görtler vortices. Phys Fluids, 2013, 25(10): 104104
31 Kim M, Choi C, Yoon D. The onset of Görtler vortices in laminar boundary layer flow over a slightly concave wall. Eur J Mech-B/Fluids, 2010, 29(6): 407–414
32 Schrader L, Brandt L, Zaki T. Receptivity, instability and breakdown of Görtler flow. J Fluid Mech, 2011, 682: 362–396
33 Boiko A V, Ivanov A V, Kachanov Y S, et al. Steady and unsteady Görtler boundary-layer instability on concave wall. Eur J Mech-B/Fluids, 2010, 29(2): 61–83
34 Ren J, Fu S. Floquet analysis of fundamental, subharmonic and detuned secondary instabilities of Görtler vortices. Sci China-Phys Mech Astron, 2014, 57(3): 555–561
35 Herbert T. Higher eigenstates of Görtler vortices. In: Müller U, Roesner K G, Schmidt B, eds. Recent Developments in Theoretical and Experimental Fluid Mechanics. Berlin, Heidelberg: Springer, 1979. 322–330
36 Floryan J M. The second mode of the Görtler instability of boundary layers. AIAA J, 1985, 23(11): 1828–1830
37 Schlichting H, Gersten K. Boundary-Layer Theory. 8th ed. Berlin: Springer, 2000
38 Schmid P J, Henningson D S. Stability and Transition in Shear Flows. New York: Springer-Verlag, 2001
39 Zhang Y, Zhou H. Verification of parabolized stability equations for its application to compressible boundary layers. Appl Math Mech, 2007, 28(8): 987–998
40 El-hady N M, Verma A K. Growth of Görtler vortices in compressible boundary layers along curved surfaces. AIAA Paper, 1981, AIAA-1981-1278
41 Whang C, Zhong X. Direct numerical simulation of Görtler instability in hypersonic boundary layers. AIAA Paper, 1999, AIAA-1999-0291
42 Benmalek A, Saric W S. Effects of curvature variations on the nonlinear evolution of Görtler vortices. Phys Fluids, 1994, 6(10): 3353–3367
43 Ren J, Fu S. Multiple Görtler modes in compressible boundary layer flows. AIAA Paper, 2012, AIAA-2012-3078
44 Ren J, Fu S. Nonlinear development of the multiple Görtler modes in hypersonic boundary layer flows. AIAA Paper, 2013, AIAA-2013-2467
45 Fu S, Wang L. RANS modeling of high-speed aerodynamic flow transition with consideration of stability theory. Prog Aerospace Sci, 2013, 58: 36–59
46 Wang L, Fu S. Development of an intermittency equation for the modeling of the supersonic/hypersonic boundary layer flow Transition. Flow Turbulence Combustion, 2011, 87(1): 165–187
47 Wang L, Fu S. Modelling flow transition in hypersonic boundary layer with Reynolds-averaged Navier-Stokes approach. Sci China Ser G-Phys Mech Astron, 2009, 52(5): 768–774